

STRONG AND WEAK LENSING UNITED III: MEASURING THE MASS DISTRIBUTION OF THE MERGING GALAXY CLUSTER 1E0657–56 *

MARUŠA BRADAČ^{1,2}, DOUGLAS CLOWE³, ANTHONY H. GONZALEZ⁴, PHIL MARSHALL¹, WILLIAM FORMAN⁵, CHRISTINE JONES⁵, MAXIM MARKEVITCH⁵, SCOTT RANDALL⁵, TIM SCHRABBACK², AND DENNIS ZARITSKY³

Draft version June 9, 2018

ABSTRACT

The galaxy cluster 1E0657-56 ($z = 0.296$) is remarkably well-suited for addressing outstanding issues in both galaxy evolution and fundamental physics. We present a reconstruction of the mass distribution from both strong and weak gravitational lensing data. Multi-color, high-resolution HST ACS images allow detection of many more arc candidates than were previously known, especially around the subcluster. Using the known redshift of one of the multiply imaged systems, we determine the remaining source redshifts using the predictive power of the strong lens model. Combining this information with shape measurements of “weakly” lensed sources, we derive a high-resolution, absolutely-calibrated mass map, using no assumptions regarding the physical properties of the underlying cluster potential. This map provides the best available quantification of the total mass of the central part of the cluster. We also confirm the result from Clowe et al. (2004, 2006a) that the total mass does *not* trace the baryonic mass.

Subject headings: cosmology: dark matter – galaxies: clusters: general – gravitational lensing – galaxies:clusters:individual:1E0657-56

1. INTRODUCTION

The cluster of galaxies 1E0657–56 is one of the hottest, most X-ray luminous clusters known. Since its discovery by Tucker et al. (1995), it has been the subject of intense and ongoing research (Mehlert et al. 2001, Markevitch et al. 2002, Barrena et al. 2002, Clowe et al. 2004, Markevitch et al. 2004, Gomez et al. 2004). In particular, Chandra observations by Markevitch et al. (2002) revealed the cluster to be a supersonic merger in the plane of the sky with a textbook example of a bow shock, making this cluster a unique case in which to study hydrodynamical properties of interacting systems. The optical images show that the cluster has two distinct components, and the X-ray analysis reveals that the lower mass sub-cluster has recently exited the core of the main cluster with a relative velocity of 4500_{-800}^{+1100} km s⁻¹. Although this relative velocity appears to be unusually large, an analysis of cosmological simulations demonstrates that it is well within the predicted range of the currently favored cosmological model (Hayashi & White

2006).

Due to its unique geometry and physical state, this cluster is the best known system in which to test the dark matter hypothesis (Clowe et al. 2004). The observed offsets between the weak gravitational lensing mass peaks and the X-ray gas component give the most direct evidence for the presence of dark matter yet available. Using the same observations, Markevitch et al. (2004) placed upper limits on the dark matter self-interaction cross section.

The goal of this work is to obtain a high-resolution, absolutely calibrated mass map with no assumptions on the physical properties of the underlying cluster potential. For this purpose we use HST ACS data, incorporating the gravitational lensing information from both multiple image systems (strong lensing) and from distortions of background sources (weak lensing). The superb spatial resolution delivered by ACS both increases the number density of background sources that can be used for weak lensing and reveals new strong lensing candidates, especially around the subcluster. The joint strong and weak lensing analysis thus benefits greatly from the ACS data, enabling us to increase the spatial resolution and signal strength of the mass map in the core of the cluster.

Encouraged by the success of the combined strong and weak lensing reconstruction method developed in Bradač et al. (2005b) (hereafter Paper I) and the results from applying the method to cluster RX J1347.5–1145 (Bradač et al. 2005a), we proceed to apply this method to 1E0657–56. Because the strong lensing data are richer in this case (RX J1347.5–1145 has not been observed with either the ACS or WFPC2 cameras prior to this study), we improve the method as described in the text.

We perform the reconstruction in the following sequence. Using ACS (multi-color where available) HST images, we identify the multiply imaged systems. Having a spectroscopic redshift for one lensed system (from Mehlert et al. 2001), we then use the predictive power

* Based on observations made with the NASA/ESA Hubble Space Telescope, obtained at the Space Telescope Science Institute, which is operated by the Association of Universities for Research in Astronomy, Inc., under NASA contract NAS 5-26555. These observations are associated with program # 10200. This work is also based in part on observations made with the Spitzer Space Telescope and with the 6.5 meter Magellan Telescopes located at Las Campanas Observatory, Chile. Spitzer is operated by the Jet Propulsion Laboratory, California Institute of Technology under a contract with NASA.

¹ Kavli Institute for Particle Astrophysics and Cosmology, P.O. Box 20450, MS29, Stanford, CA 94309, USA

² Argelander-Institut für Astronomie, Auf dem Hügel 71, D-53121 Bonn, Germany

³ Steward Observatory, University of Arizona, 933 N Cherry Ave., Tucson, AZ 85721, USA

⁴ Department of Astronomy, University of Florida, 211 Bryant Space Science Center, Gainesville, FL 32611, USA

⁵ Harvard-Smithsonian Center for Astrophysics, 60 Garden Street, Cambridge, MA 02138, USA

Electronic address: marusa@slac.stanford.edu

of simple strong lens modeling to estimate the redshifts of the other systems. Using positions and redshifts of the strongly lensed images and the shape measurements of the “weakly” lensing sources, we perform a combined strong and weak lensing mass reconstruction, thereby significantly improving the constraints on the mass and positions of the main cluster and the colliding subcluster of 1E0657–56. In terms of the structure of this paper, in section 2 we describe the optical images used in this analysis, the basic image processing and the extraction of the strong (§2.1) and weak (§2.2) gravitational lensing data. We then infer the mass distribution of cluster 1E0657–56 from these data in section 4, following a demonstration of our methodology on suitable simulated data in section 3. We discuss the possible sources of error in section 5 and summarize our conclusions in section 6.

2. OBSERVATIONS AND DATA REDUCTION PROCESS

ACS/WFC imaging of the cluster 1E0657–56 was carried out in Cycle 13 (proposal 10200, PI Jones) on 2004 October 21 in two pointings with one and three different filters respectively. The two pointings are centered on the main cluster and the subcluster with a small overlap between them. The subcluster was observed in three different filters (three orbits with F814W, one with F606W, and one with F435W), while the main cluster was observed only in the F606W filter (one orbit).

The demands placed by the lensing analysis require special care when reducing the images. We use the *Multidrizzle* (Koekemoer et al. 2002) routine to align the images. To register the images with the astrometric accuracy needed for lensing analysis, we determine the offsets among the images by extracting high S/N objects in the individual, distortion corrected exposures. We use *SExtractor* (Bertin & Arnouts 1996) and the IRAF routine *geomap* to identify the objects and calculate the residual shifts and rotation of individual exposures, which were then fed back into *Multidrizzle*. We use “square” as the final drizzling kernel and an output pixel scale of 0.03 arcsec; this is smaller than the original pixel scale of the ACS CCD to reduce the impact of resampling on the shape measurements.

2.1. Strong lensing image identification

Owing to its complex structure, the strong lensing analysis of the 1E0657–56 cluster is complicated. Among the multiply-imaged systems, only the giant arc on the NW side of the main cluster’s cD has a measured redshift ($z = 3.24$ Mehlert et al. 2001). Corresponding images for multiply-imaged sources were identified by matching both morphologies and surface brightnesses in each of the available ACS bands (F435W, F606W, and F814W) and ground-based filters, BVR data from Magellan and I-band from VLT (Clowe et al. 2004).

We confirm (based on photometry and morphology) that the 6 systems (labeled A-F in Table 1) previously identified by Mehlert et al. (2001) are indeed multiply imaged. We identify four additional systems (G-J) in the subcluster region, where none were previously known. All of these are identified in Fig. 1, and image positions (corresponding to the peak surface brightness) are presented in Table 1. Unfortunately, for the greater part of the main cluster, only a single band ACS image is available, which makes identification of additional candidates

significantly more ambiguous.

Using these identifications, we perform a parametrized strong lensing reconstruction. At this stage we are not generating a detailed strong lensing model, rather we use this parametrized model only to predict the redshifts of the systems where spectroscopic redshifts are not available (all systems but A) and as the initial model guess for the subsequent strong and weak lensing reconstruction. For this reconstruction, we use only the image positions as constraints. The parametrized model consists of two non-singular isothermal ellipses (NIE) (Keeton & Kochanek 1998), for which the scaled surface mass density κ is given by

$$\kappa(\vec{\theta}) = \frac{b}{2\sqrt{\frac{1+|\epsilon_g|}{1-|\epsilon_g|}(r_c^2 + (\theta_1)^2) + (\theta_2)^2}}. \quad (1)$$

$\vec{\theta}$ is defined counterclockwise from due west and b is related to the line-of-sight velocity dispersion σ through $b \propto \sigma^2$. The components are centered on the southern cD galaxy of the main cluster and the brightest cluster galaxy (BCG) of the sub cluster respectively (denoted with white crosses in Fig. 1; it is not straightforward to identify the BCG of the main cluster, therefore we refer to the two main galaxies as the southern and northern cD). We allow the scaling b , core radii r_c , ellipticities $|\epsilon_g|$, and position angles ϕ_g of these to vary.⁷ Following the prescription of Kneib et al. (1996), we also include the 20 brightest cluster members from the F606W-band (selected using color information from Magellan data) in the mass model. The galaxies are modeled as non-singular isothermal spheres with a line-of-sight velocity dispersion σ_{memb} and core radius $r_{c,\text{memb}}$ following

$$\sigma_{\text{memb}} \propto L^{1/4}, r_{c,\text{memb}} \propto L^{1/2}, \quad (2)$$

The proportionality constants are allowed to vary as well and below we quote the values of σ_{memb} and $r_{c,\text{memb}}$ for a fiducial galaxy with a F606W-band magnitude $m_{\text{F606W}} = 18$. The best fit model for this system has values of $\{\sigma, r_c, |\epsilon_g|, \phi_g\} = \{1300 \text{ km s}^{-1}, 0.3', 0.2, 45^\circ\}$ for the main cluster, $\{\sigma, r_c, |\epsilon_g|, \phi_g\} = \{1000 \text{ km s}^{-1}, 0.3', 0.2, 280^\circ\}$ for the subcluster, and $\{\sigma_{\text{memb},18}, r_{c,\text{memb},18}\} = \{250 \text{ km s}^{-1}, 0.3'\}$ for the cluster members. We also allow the redshifts of systems B-J to vary. The resulting best fit redshifts are given in Table 1. To evaluate the angular diameter distances throughout the paper we assume the Λ CDM cosmology with $\Omega_m = 0.3$, $\Omega_\Lambda = 0.7$, and Hubble constant $H_0 = 70 \text{ km s}^{-1} \text{ Mpc}^{-1}$.

For objects close in projection to the main cluster, the redshift estimates are fairly reliable because the well-measured arc A is located there (we estimate an error of $\Delta z = 0.2(1+z)$). However, the redshift estimates for those close to the subcomponent are less well-determined, and are somewhat degenerate with the adopted mass of the subcluster. We postpone an extension of the methodology described in the following sections that incorporates simultaneous solution for the unknown source redshifts to future work, but here note

⁷ We define all ellipticities ϵ throughout this paper as in Bartelmann & Schneider (2001) with $|\epsilon| = (1-f)/(1+f)$, f being the axes ratio.

TABLE 1
THE PROPERTIES OF THE
MULTIPLY-IMAGED SYSTEMS USED IN
THIS WORK.

	Ra	Dec	z_{pred}
A	104.63316	-55.941395	3.24 ^a
	104.62988	-55.943798	
B	104.62954	-55.941844	4.8
	104.63042	-55.941474	
C	104.63775	-55.941851	2.1
	104.63338	-55.945324	
D	104.64709	-55.943575	1.4
	104.63528	-55.951836	
E	104.64008	-55.950620	1.0
	104.64232	-55.948784	
F	104.65155	-55.956671	0.8
	104.64778	-55.958284	
G	104.56568	-55.939832	1.3
	104.56402	-55.942113	
H	104.56417	-55.944131	1.9
	104.56293	-55.939764	
I	104.56133	-55.942430	2.1
	104.56189	-55.947724	
J	104.56186	-55.946114	1.7
	104.56052	-55.942930	
	104.56141	-55.944264	
	104.56909	-55.946016	

^aThe redshift of arc A was determined spectroscopically by Mehlert et al. (2001). Other redshifts are determined using the best-fit strong lensing model.

that: 1) the parametrized model allows the generation of a set of source redshifts that, while model-dependent, are self-consistent; 2) the predicted redshifts are consistent with the colors of the objects. We adopt the redshifts estimated here for the combined strong and weak lensing reconstruction, and where possible estimate the systematic error introduced as a result of this simplification.

2.2. Weak lensing catalogs

In the weak lensing analysis, we use the F435W, F606W, and F814W exposures for the subcluster, and F606W wherever multicolor ACS data are not available. We will only outline the main steps used for this analysis, full details on how the weak lensing catalogs were generated will be given in a future paper dealing with the weak lensing mass measurements of 1E0657–56 at large radius (Clowe et al. 2006c, in prep.).

We correct galaxy images for the PSF anisotropy and PSF smearing closely following the technique described in Clowe et al. (2006b). The procedure is based on the KSB algorithm (Kaiser et al. 1995), in particular we use the modified IMCAT implementation. The KSB method is formally valid only in the weak lensing regime (i.e. at radii much larger than where multiply imaged systems form and where the distortions are small). However recent simulations from the STEP project (Heymans et al. 2006) show that this approach is also valid in the non-weak lensing regime (i.e. with shear values of $|\gamma| \sim 0.1 - 0.3$) to the accuracy needed for a single cluster reconstruction. Lastly, in the vicinity of the highly elongated arcs we are dominated by the strong lensing signal,

thereby minimizing the effects of signal dilution due to imperfect PSF correction.

We select stars from the half-light-radius vs. magnitude diagram and fit a fifth order polynomial to their measured ellipticities as a function of their position on the drizzled image. After the correction the rms of the stellar ellipticity components ϵ_1 and ϵ_2 (as defined in Bartelmann & Schneider (2001)) changes from 0.017 to 0.015 and from 0.004 to 0.003, respectively, and the mean is shifted to 0 in both cases. The shear is then measured independently in all available filters and a weighted average is calculated from those to arrive at our final, PSF corrected ellipticity estimates. We use the $\sim 1'$ overlap between the two F606W pointings to test for systematics in the PSF correction. The differences in the shears derived from the two exposures is consistent given the noise level.

The ACS camera has a PSF that varies both spatially and temporally. While the approach described above accounts for the spatial dependence, it does not account for time variations. We investigate the PSF time dependence by measuring stellar shapes in individual exposures (four exposures were taken within each orbit). We conclude that the PSF is *not* stable (i.e. the global pattern of the PSF changes) even within a single orbit. However our detected signal is much stronger than the typical residuals due to imperfect PSF removal caused by the temporal variation; therefore we use the combined images to measure shapes. In addition, the PSF shape of an individual star changes as a function of its radius (see e.g. Heymans et al. 2005, Jee et al. 2006); we therefore match the radius used to measure the stellar correction factors with that for the galaxies. Using simulated weak lensing data we identified a constant bias between the measured and estimated shear values; this bias was calculated for each image set separately and was introduced as a multiplicative shear calibration factor when producing final catalogs.

The color cuts applied to each catalog to remove cluster and foreground galaxies were color-color cuts estimated using photometric-redshift templates of galaxies at redshifts $z \lesssim 2$. We used templates of all but extreme starburst galaxies, under the assumption that there are not likely to be many faint, low-redshift starburst dominated galaxies, particularly in a cluster. As such, we expect that unless there is an unknown population of dwarf galaxies in the cluster with colors much different from known populations, we will have removed all but a handful of outliers (extreme starbursts or dust obscured). We only use objects which were detected in more than a single band; in particular we reject all the objects that are detected only in the F606W pointing of the main cluster and were too faint for detection in the Magellan images.

Unfortunately the observations at hand do not allow us to determine the photometric redshifts of the sources used for weak and strong lensing. We would need at least NIR data to reliably determine the redshifts, as most of the sources are located at $z \sim 1$. Therefore following Clowe et al. (2006b), we estimate the redshifts of the background sources by applying the color and magnitude cuts that remove the likely foreground population to the HDF-S photometric redshift catalog of Fontana et al. (1999). For the remaining sources, we average the ratios

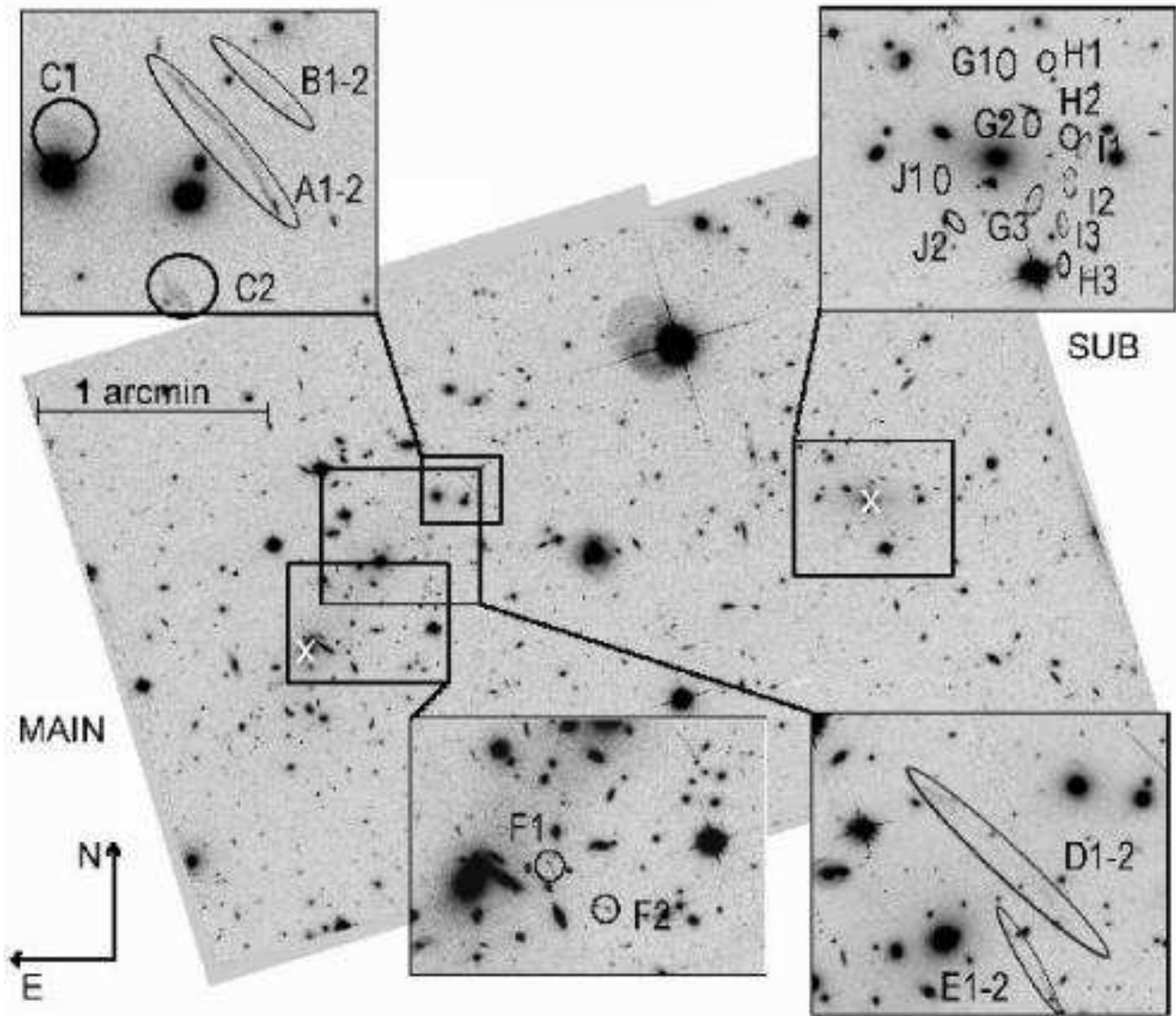


FIG. 1.— The two F606W pointings of the main and sub component region of 1E0657–56. Multiply imaged systems are marked and labeled (see also Table 1). White crosses denote the positions of the southern cD of the main and BCG of the subcluster.

$D_d D_{ds}/D_s$ (where D_d , D_s , and D_{ds} are the angular diameter distances to the cluster, source and between the cluster and the source respectively) to generate a very crude estimate of the individual redshifts, but good average redshifts per population (provided the redshift distribution of the HDF-S is representative of that of our background sources). As a result all of the galaxies in a certain magnitude bin will be given the same redshift. The main reason of this approach, instead of calculating a mean for the whole catalog is the fact that the images have different depths in different parts of the reconstructed area, and this method allows us to account for the sudden jumps in the mean background galaxy redshift across the image boundaries, which would otherwise introduce spurious features in the reconstructions.

This method is only approximate, therefore we test the reconstruction method using mock catalogs with only

limited knowledge of the redshift of the source population in Sect. 3. The weak and strong lensing reconstruction performs well under these conditions. In addition, any significant dilution of the signal will be compensated by the strong lensing signal (if more than one strong lensing system is used). The cluster is also at a moderate redshift, therefore changing the sources from redshifts of $z = 1$ to $z = 1.5$ would change the lensing strength by $\sim 14\%$. In conclusion we expect the contributions due to errors in the assumed distribution of $D_d D_{ds}/D_s$ to be smaller than that expected from the galaxy ellipticity shot noise.

Finally, we fit the non-singular isothermal sphere NIS model to the averaged tangential ellipticities $\langle \epsilon_t \rangle$. Both components generate large tangential shear signal. We center circular bins on the southern cD of the main cluster and the BCG of the subcluster. The resulting NIS

fit for the main cluster results in $\sigma_{\text{NIS}} = 1300 \text{ kms}^{-1}$, $x_{c,\text{NIS}} = 0.4$, and $\sigma_{\text{NIS}} = 1000 \text{ kms}^{-1}$, $x_{c,\text{NIS}} = 0.6$ for the subcluster. This is an oversimplified model because the cluster is morphologically disrupted and we do not correct for the contamination of the main cluster profile in the sub cluster region (and vice versa).

3. STRONG AND WEAK LENSING RECONSTRUCTION FROM HIGH RESOLUTION (ACS) DATA

Our strong and weak lensing reconstruction is performed using the method described in Paper I. The main idea behind the method is to describe the cluster mass distribution using a set of generic model parameters, which we choose to be the projected gravitational potential ψ_k measured on a regular square grid. The total χ^2 is defined as

$$\chi^2(\psi_k) = \chi_\epsilon^2(\psi_k) + \chi_M^2(\psi_k) + \eta R(\psi_k). \quad (3)$$

where $\chi_\epsilon^2(\psi_k)$ is the contribution from weak lensing, $\chi_M^2(\psi_k)$ from strong lensing and $R(\psi_k)$ is the regularization function with regularization parameter η . We closely follow the methodology presented in Paper I, with the few differences described below.⁸

The most important difference is that we extend the formalism to more than a single set of multiple images. This may appear straightforward because we only need to sum up the contributions to χ_M^2 from each system. Given N_S multiply imaged systems having N_i images each, we define χ_M^2 as

$$\chi_M^2 = \sum_{i=1}^{N_S} \sum_{m=1}^{N_i} \vec{b}_{m,i}^T \mathcal{S}^{-1} \vec{b}_{m,i}, \quad (4)$$

where \mathcal{S} is the covariance matrix and $\vec{b}_{m,i} = \vec{\theta}_{m,i} - Z(z_{s,i})\vec{\alpha}(\vec{\theta}_{m,i}) - \vec{\beta}_{s,i}$. $\vec{\beta}_{s,i}$ is the average position of the i -th source (calculated from the image positions and given the deflection angle $\vec{\alpha}$), and $Z(z_{s,i})$ is the so-called ‘‘cosmological weight’’ function as defined in Bartelmann & Schneider (2001).

In Paper I we assumed that the covariance matrix is diagonal and independent of the lens model parameters. As discussed in e.g. Kochanek (2004), this approach is not optimal and can lead to solutions that are biased toward models that predict high magnification at the image positions. With more sources at differing redshifts, this problem becomes more apparent because the method likely converges toward a solution with steep gradients in the surface mass density close to image positions (allowing for the ‘‘fine tuning’’ of the reconstruction). To overcome such unphysical solutions, we use a better approximation for the error containing the magnification at the image position $\mu(\vec{\theta}_{m,i})$ and obtain the covariance matrix $\mathcal{S} = \left| \mu(\vec{\theta}_{m,i}) \right|^{-2} \text{diag}(\sigma_{s,1}^2, \sigma_{s,2}^2)$. Such a procedure is approximately correct, provided we are close enough to the true model (see Kochanek 2004). The covariance matrix is still diagonal; however we argue that assuming it to be such in the source plane is in fact a better approximation than assuming the covariance matrix to be

diagonal in the image plane, as sources are on average more circular than their lensed images. In addition, in practice multiple image constraints are satisfied nearly perfectly and exact values of errors on image positions are of lesser importance.

We adapt the method to accommodate data regions of arbitrary size and shape, but the potential is reconstructed only in grid cells containing weak and/or strong lensing data. We tile the observed field with a regular grid and determine which cells contain either weak lensing galaxies or multiple images. This can result in some cells being sparsely populated (holes in the data, edge effects), but the regularization ensures that potential is properly reconstructed. Once the data-grid is determined, we ensure that each of the data grid points is surrounded by a 4×4 grid of points that are included in the reconstruction to calculate the scaled surface mass density κ , shear γ , and the deflection angle $\vec{\alpha}$, using finite differencing, as described in Paper I.

To find the χ^2 -function minimum, we search for a solution of the following system of equations $\frac{\partial \chi^2(\psi_k)}{\partial \psi_k} = 0$. This is in general a non-linear set of equations, which we solve in an iterative manner. We again linearize this system as described in Paper I, calculating all of the non-linear terms (for the strong lensing term in particular these are now the ones containing $\vec{\beta}_{s,i}$ and $\mu(\vec{\theta}_{m,i})$) using the information from the previous iteration. We regularize the solution using a ‘‘moving prior’’, gradually updating our knowledge of the model by increasing its complexity and computing its likelihood relative to the previous (simpler) model. We begin with an initial model ($\kappa^{(0)}$, $\gamma_1^{(0)}$, $\gamma_2^{(0)}$) computed on a relatively coarse grid, and then gradually increase the number of grid points, comparing the resulting κ map with that from the previous iteration, linearly interpolated onto the finer grid. In addition to κ we now also use the components of the shear γ_1 and γ_2 in the regularizing scheme, to avoid the numerical effects described in Paper I even more efficiently. The regularization constant was set after experimentation with simulated data. When using many multiply imaged systems, the final reconstruction is even less sensitive to these choices than when only a single system is used (as in Paper I); we discuss this finding in more detail in Sect. 5.

With many multiply imaged systems, we must choose a sufficiently fine grid to be able to calculate the difference in the deflection angle between images of different systems (if images from more than one system lie within the same grid cell, it is difficult to find a good solution). Ideally one would like to use adaptive grids for this purpose (having a relatively coarse grid where only weak lensing information is available and increasing the resolution in the vicinity of the multiple images). Unfortunately it is computationally difficult to track such a problem and is therefore beyond the scope of this paper, but will be a subject of future work.

We tested all the improvements described above using a high-resolution N-body simulation of a galaxy cluster by Springel et al. (2001). The catalogs are generated as in Paper I, although adapted to the higher-resolution data that we use here. The weak lensing simulated data are obtained by placing 1800 galaxies (giving a den-

⁸ In figure 2 in Paper I the factor of $\frac{1}{2} \frac{1}{6}$ in finite differencing formula for κ is wrong. All the calculations in all three papers do however use the correct factor of $\frac{1}{6}$.

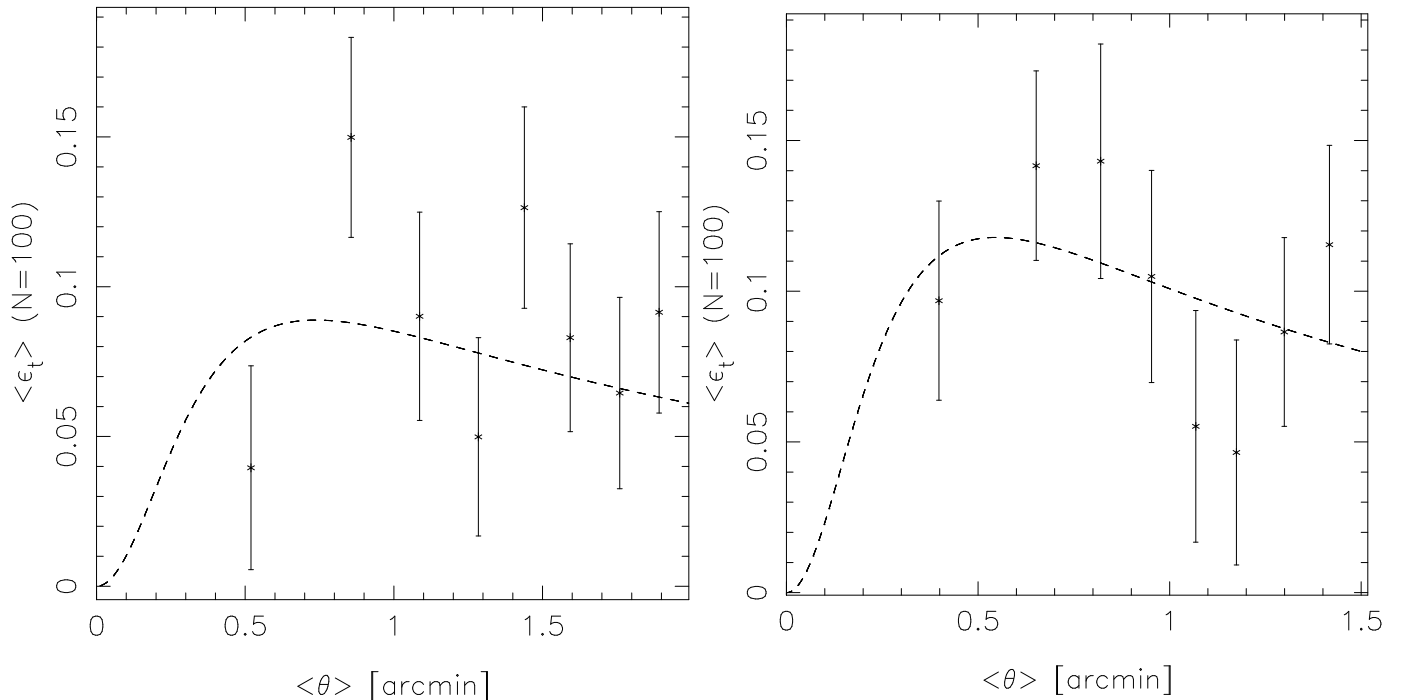


FIG. 2.— Average tangential ellipticity $\langle \epsilon_t \rangle$ vs. projected radius $\langle \theta \rangle$ in radial bins centered on the southern cD of the main cluster (*left panel*), and the BCG of the subcluster (*right panel*) containing 100 galaxies per bin. The errors are obtained by randomizing the phases of the measured ellipticities, while preserving their absolute values. 100 realizations are performed. The dashed line shows the best-fit non-singular isothermal sphere (NIS) profile to the binned data (see text). It is plotted here for the average source redshift of weak lensing sources $\langle z \rangle = 1.0$.

sity of 120 arcmin^{-2}) randomly on a $3.8 \times 3.8 \text{ arcmin}^2$ field. The intrinsic ellipticities ϵ_s are drawn from a Gaussian distribution, with each component characterized by $\sigma = \sigma_{\epsilon_s} = 0.2$. We then draw the redshifts of the background sources, following Brainerd et al. (1996), from a gamma distribution $p_z(z) = z^2 / (2 z_0^3) \exp(-z/z_0)$ with $z_0 = 1/3$, giving a mean redshift of $\langle z \rangle = 3z_0 = 1$, and a mode of $z_{\text{mode}} = 2z_0 = 2/3$. We reject the foreground objects, and use the background object redshifts when predicting the lensed shapes. However, when using the catalogs for the reconstruction, we assume *no* knowledge of the individual redshifts: instead all sources are assumed to have $z = 1$, in agreement with the poor estimates available for the actual data. The multiple-image systems are generated as described in Paper I. Four quadruply-imaged systems are generated at source redshifts of $z_s = \{0.8, 1.0, 3.0, 5.0\}$. The initial model for the regularization is set to $\kappa^{(0)} = \gamma_1^{(0)} = \gamma_2^{(0)} = 0$.

The resulting reconstruction is given in Fig. 3. It is very encouraging to observe how well the overall shape (the agreement in the ellipticity and position angle of the main component, and the overall profile) and its mass are reconstructed. These successes would not be possible with weak lensing data alone, owing to the mass-sheet degeneracy (i.e. the reconstruction would suffer from the degeneracy of the form $\kappa \rightarrow \kappa' = \lambda\kappa + (1 - \lambda)$, where λ is an arbitrary constant, see e.g. Bradač et al. 2004). In addition with the ACS-quality data, we are starting to resolve the small-scale substructure of the potential.

4. CLUSTER MASS RECONSTRUCTION OF 1E0657–56

We now apply the above mentioned reconstruction method to the strong and weak lensing data of 1E0657–56. As described in Sect. 2.1, we use 10 distinct multiply imaged systems and $N_{\text{gal}} \sim 1900$ “weakly” lensed galaxies (120 arcmin^{-2}). We start with a $30 \times 30 \text{ pix}^2$ grid for a $7 \times 7 \text{ arcmin}^2$ field oriented with respect to the negative RA coordinate (not all of the grid cells contain data and those that do not are excluded from the reconstruction). We gradually increase the number of grid points (for reasons described in Sect. 3) in steps of 1, with the final reconstruction performed on a $60 \times 60 \text{ pix}^2$ grid. In our initial model, we use a two-component NIE model with parameters as given in Sect. 2.1 to set the regularization. The possible dependence of the reconstruction on initial conditions is discussed in the next section.

The resulting reconstruction is shown in Fig. 4, together with X-ray surface brightness contours from the 500 ks Chandra observation. The two cluster components are clearly detected. In addition, with superb strong lensing data (due to exquisite ACS resolution and multi-color information for the subcluster) we are starting to resolve multiple components within each individual system.

From this reconstruction, we measure the enclosed (projected within a cylinder) mass for this system. The main cluster has $M_{\text{main}}(< 250 \text{ kpc}) = (2.8 \pm 0.2) \times 10^{14} M_{\odot}$, while the sub cluster has $M_{\text{sub}}(< 250 \text{ kpc}) = (2.3 \pm 0.2) \times 10^{14} M_{\odot}$ ($1 \text{ arcmin} = 260 \text{ kpc}$ at the cluster redshift). The mass errors represent combined errors obtained by bootstrap resampling of the weak lensing catalogs, performing a similar experiment for the strong lens-

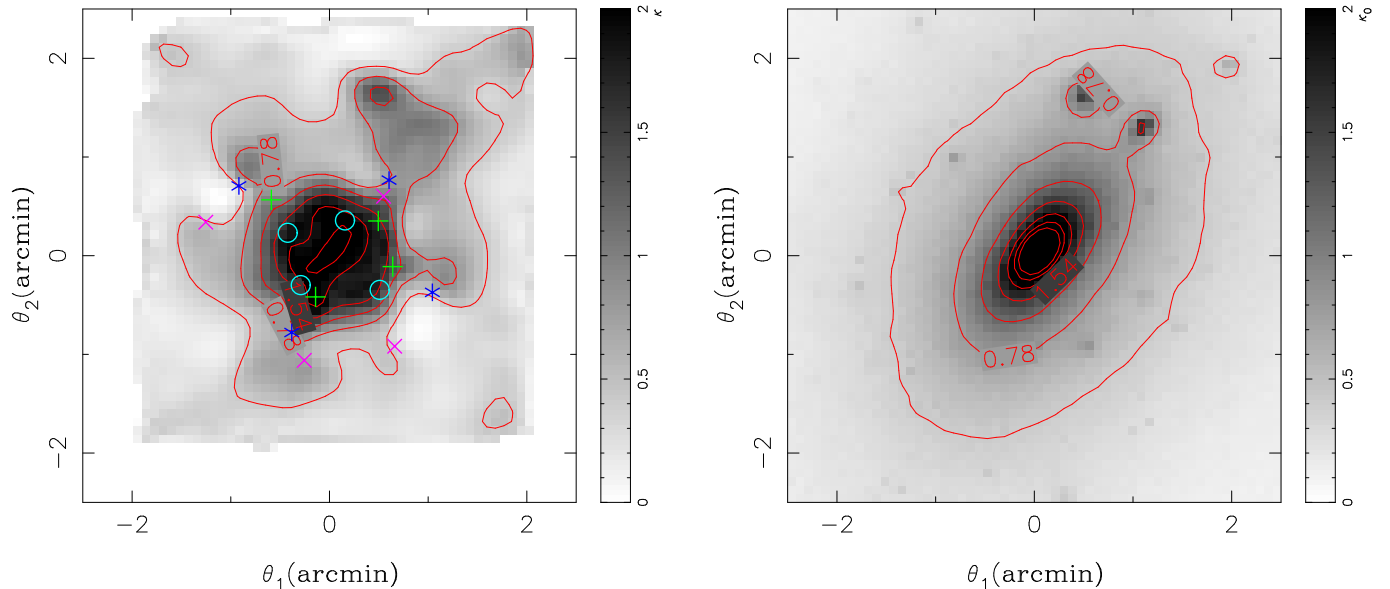


FIG. 3.— The reconstructed (left) and the original (right) surface mass density κ of the simulated cluster described in section 3. The symbols in the left panel denote the image positions of the four multiple-image systems at $z_s = \{0.8, 1.0, 3.0, 5.0\}$ which we use for the reconstruction. The contour levels, which are the same in both panels, are linearly spaced with $\Delta\kappa = 0.38$, starting at $\kappa = 0.4$ for a fiducial source at infinite redshift, $z_s \rightarrow \infty$.

ing data, and estimating systematic uncertainties from the mass differences obtained using different initial models (see discussion in the next section). We plot the integrated, azimuthally-averaged mass profiles $M(< R)$ for the two components in Fig. 5. We fit power-law models ($M(< R) \propto R^{n_i}$) to these profiles, and find logarithmic slopes of $n_{i,\text{main}} = 0.8$ for the main cluster and $n_{i,\text{sub}} = 1.1$ for the subcluster. In terms of the surface mass density $\kappa(r) \propto r^{-n}$, this translates to $n_{\text{main}} = 1.2$, and $n_{\text{sub}} = 0.9$. Adopting an isothermal profile ($n = 1$), we find the line of sight velocity dispersions for the main and the sub cluster are $\sigma_{\text{main}} = (1400 \pm 100) \text{ km s}^{-1}$ and $\sigma_{\text{sub}} = (1200 \pm 100) \text{ km s}^{-1}$ respectively; in good agreement with the analysis in Sect. 2.2. However, as already mentioned in that section, given the size of the errors, the asphericity of the system, and the complicated geometry (the relative contributions of the main and sub cluster are difficult to disentangle), the velocity dispersion and slope measurements should only be used as guidelines.

Because of this cluster’s violent history, we can not expect the assumption of isothermality to hold. Therefore (and for the reasons stated above) it is also non-trivial to compare our velocity dispersion measurements with the ones from Barrena et al. (2002). Their estimate for the main cluster agrees with ours, while the velocity dispersion of a subcluster is much lower in their case. An isolated lens with the low velocity dispersion measured by Barrena et al. (2002) for the subcluster would have multiply imaged systems only at radii $\lesssim 1''.3$, a factor of ~ 8 below that observed. The influence of the main cluster can increase the radial range over which multiple images exist, but not to the extent observed here. We conclude that the true velocity dispersion of the subcluster is likely to be smaller than that derived from our mass model (due to the inclusion of mass from the main cluster), but larger than that presented by Barrena et al.

(2002).

One of the important results of the work of Clowe et al. (2004, 2006a) was the measurement of the offset between dark matter and baryons. We confirm these results: our strong and weak lensing offsets for the mass peaks (by measuring the peaks in κ -distribution) and the corresponding errors are given in Table 2. To estimate the significance of this offset we also measured the positions of the two peaks (for the main and the subcluster) in each of the 1000 reconstructions using the bootstrap resampled weak lensing catalogs (described below). In none of these realizations are the mass peaks coincident with the corresponding X-ray peaks. The $1\text{-}\sigma$ error bars are a factor of 10 and 6 smaller than the offsets for the main and subcluster respectively. If these errors are accurate and Gaussian distributed, this result translates into $10\text{-}\sigma$ and $6\text{-}\sigma$ discrepancies between the corresponding gas and the total mass peaks. These offsets directly demonstrate that dark matter is present and is the dominant mass component of this cluster.

Lastly, we compare the projected gas mass (the details of modeling will be given in Randall et al. 2006) vs. the total mass within elliptical regions centered on the two peaks of the X-ray emission and the southern cD of the main and BCG of the subcluster, respectively (see Table 3). The ratio of gas mass to total mass is smaller in the regions centered on the massive galaxies rather than the X-ray peaks, indicating that the gas has been (to some extent) stripped, and is no longer coincident with the total mass. In addition, we detect an extension in the total mass map to the NW of arc A. This detection can be partly attributed to the hot X-ray gas (see Fig. 4).

5. POSSIBLE SYSTEMATIC EFFECTS

To assess the reliability of the reconstructed map, we generate 1000 bootstrap resampled weak lensing catalogs

TABLE 2
OFFSETS (WITH $1\text{-}\sigma$ ERRORBARS) OF THE MASS PEAKS
AND GAS PEAKS FROM THE CORRESPONDING SOUTHERN
CD OF THE MAIN AND BCG OF THE SUBCLUSTER
(MARKED WITH CROSSES IN FIG. 1).

	Δx ([arcmin])	Δy ([arcmin])
Main component	0.26 ± 0.08	-0.01 ± 0.09
Main component (gas)	1.06	0.84
Sub component	-0.05 ± 0.10	0.00 ± 0.07
Sub component (gas)	-0.73	0.10

and perform reconstructions on each of these. To further test the reliability of the strong lensing data we create 10 different reconstructions each time removing one of the multiply imaged systems we use. The resulting κ -maps do not change substantially, the main features (i.e. the ellipticity of the main and the subcluster) seen in Fig. 4 remain in all of the reconstructions.

We also perform a reconstruction using the weak lensing data only (bottom-left panel of Fig. 6). From only weak lensing, we clearly detect both the main and sub clusters, but are unable to resolve individual substructures within each with high significance. This failure can in part be attributed to the limited field size used here in contrast to Clowe et al. (2006a) (our method at present does not allow us to use larger fields for the reconstruction, adaptive grid methods need to be employed then). In addition, the mass estimates from weak lensing reconstruction are unreliable (due to the mass-sheet degeneracy); the resulting potential does not reproduce any of the multiply imaged systems observed. Traditionally, to overcome the problem of the mass-sheet degeneracy and measure the mass from the weak lensing mass reconstruction, one assumes a vanishing surface mass density at the edge of the field or adopts parametrized model fitting. The former is not applicable here because the field used is too small. The latter will yield reliable mass estimates if the assumed profile is correct, but it is difficult to guess the appropriate model for such a morphologically disturbed cluster. Combining strong and weak lensing helps us to break this degeneracy. However, the lack of counter arc candidates and redshifts of multiply imaged systems limits our ability to provide even stronger constraints on the mass distribution.

The errors on mass estimates quoted throughout the paper are obtained by summing in quadrature the errors obtained from the reconstructions using bootstrapping of the weak lensing catalogs and removing individual strong lens systems. In addition, we estimate and add systematic uncertainties resulting from differences in the reconstruction when using different initial models (as explained below). In principle, we should incorporate all of these effects simultaneously in the reconstructions, however this is too computational intensive and beyond the scope of this analysis.

5.1. Initial conditions

Methods involving strong lensing mass reconstruction with many multiple imaged systems are subject to degeneracies in parameter space. It is difficult to search the parameter space because the χ^2 function has many

local extrema. In our case, there are pronounced, narrow secondary minima where individual systems are reconstructed well by the model (and the others less so) and high “walls” in χ^2 space where images happen to form close to the corresponding critical curves. Because weak lensing data are noisy, additional, though less pronounced, minima in χ^2 are created. Given that our reconstruction method does not guarantee that we find a global minimum, in principle we would need to check the whole parameter space. This search is unfeasible with any available algorithms, given that the number of parameters (i.e., pixels in the mass map) is > 1000 .

Instead, we opt to investigate the use of many initial models. We try both extremes; i.e. models that are clearly in disagreement with the data (zero initial conditions, single mass peak centered on the position of the gas) and models that use alternative methods to reconstruct the data (two-NIE model, two-NIE plus cluster members model from strong lensing modeling, weak lensing mass model from Clowe et al. 2006a). Although the details of the reconstruction depend on the initial conditions (as can be seen from comparing all but bottom-right κ -maps in Fig. 6), the main features (SE-NW elongation of the main cluster, two mass peaks close to the main cluster cDs, an elongation in the mass map toward the gas peak, E-W elongation of the subcluster) are independent of the particular initial model we use.

The resulting χ^2 contribution of the weak lensing data χ^2_ϵ remains the same for all sets of initial conditions ($\chi^2_\epsilon \simeq 7000$ for $2N_{\text{gal}} = 3800$ data points). The strong lensing contribution is lowest when the two component NIE model is used ($\chi^2_M = 20$) and highest when the zero model initial conditions ($\chi^2_M = 1000$) are used. Although the absolute values of the χ^2 have little meaning (i.e. one can change the regularization parameter to obtain a lower value for χ^2_ϵ because the weak lensing data is noisy), the relative values tell us which resulting reconstruction is indeed a better fit to the data (as the same regularization parameters are used in all cases and it is the fit to the high signal to noise strong lensing data that improves).

We estimate the systematic uncertainty on our mass estimates by calculating the maximum difference in the resulting mass estimates when using different initial models. We exclude the zero model in this calculation as it does not predict the strong lensing data reliably. The resulting κ -map (see bottom-left panel in Fig. 6) for this model is suppressed where only weak lensing data are available (due to the mass-sheet degeneracy) and produce steep gradients close to arc A and a $\sim 10\%$ lower overall mass. However, other features in the reconstruction (positions and shapes of the mass peaks for the main and the sub-cluster) remain unchanged. In all cases, the resulting mass peaks “move” away from the initial guess; showing that the regularization is sufficiently flexible to reproduce the features in the data. Therefore, we are confident that our results are not biased as a result of the particular choices of regularization and are independent of the initial conditions to the extent presented in Fig. 6.

5.2. Strong-lens system identification and redshifts

Finally, the mass measurements presented above depend on the reliability of the redshifts and identification

used for strong lensing reconstruction. These (except for system A) are not secure and depend upon the model used in Sect. 2.1. In particular, the redshifts of the systems around the subcomponents (and consequently the measurements of its mass) can change because the subcomponent mass reconstruction does not depend strongly on the modeling around the main component (where the arc with the known redshift is located).

The parametrized model used in Sect. 2.1 to estimate the redshifts of the strong lensing systems likely deviates from the truth model. We tested the dependence of the assumed redshifts by performing 100 reconstructions in which we modified all of the strong lensing system redshifts except for system A. For each reconstruction these uncertain redshifts were changed by assuming a Gaussian scatter with $\sigma_z = 0.5$ and requiring that all sources lie behind the cluster. The resulting mass and position errors were smaller (by a factor of ~ 2) than the ones quoted throughout the paper, and the mass and position measurements were unbiased (as expected from such an analysis). The mass measurements would change, however, if we systematically increase (decrease) the redshifts of all the systems. For example, if we decrease the redshifts of the subcluster systems such that the lowest redshift system of the subcluster (G) is at $z_s = 0.5$ (and scale the others accordingly), then the mass increases by a factor of $\sim Z(1.3)/Z(0.5) = 2$. If we instead increase all the redshifts, pushing the highest redshift system (I) to $z = \infty$, then the mass of the subcluster will decrease by $1.0/Z(2.1) = 1.2$. Note however that these are just estimates, since the redshift estimates of the weak lensing sources also plays a role, and the changes will therefore be even smaller.

As a further test, we also perform 10 reconstructions where we remove one strong lens system at a time from the analysis. In Fig. 7 we show the two that differ the most from the reconstruction that uses all the strong lensing systems. When we remove system I from the reconstruction (right panel in Fig. 7) the double peaked structure of the subcluster disappears, while the east-west elongation remains. For the main cluster we see the largest deviations from the original map when we remove system D from the reconstruction (left panel in Fig. 7). However, these results do not mean that these structures are not real, rather they illustrate some possible systematics when dealing with sparse strong lensing data. We are confident that system D is indeed multiply imaged, and images I2-I3, at least, are also probably multiply imaged.

These tests demonstrate that even though the strong lensing system identification and their redshift determinations are important to the details of the reconstruction, the errors arising from misidentifications/redshift misestimation are within those quoted in the previous section.

5.3. Predictive power of the model

The predicted redshifts and strong lensing system identification can be tested using spectroscopy. We are planning just such a survey and will therefore be able to test the fidelity of our model in the future. In addition, using Spitzer IRAC data we identify a candidate high redshift object. While bright in all IRAC bands, the faintness of this galaxy in optical and near infrared bands indicates that it could lie at $z \gtrsim 6$. It has two components

and our predicted critical curve for this redshift (indistinguishable from the $z \rightarrow \infty$ critical curve) is exactly where it should be if indeed these sources are merging images of the same source; they are denoted with crosses and plotted together with the critical curve in Fig. 8. Furthermore, we identify a candidate counter image with similar colors in the IRAC data just outside the critical curve. All three need to be further analyzed and confirmed (using spectroscopy and/or NIR data) before we include them in the modeling.

We also identify possible counter-images for systems B, J, H, and I as predicted from our model, they are indicated in Fig. 9. If these and high-redshift candidate are confirmed, the predictive power of our model would further indicate that the strong lensing data we use is reliable enough for this work.

6. CONCLUSIONS AND FUTURE WORK

Massive and interacting clusters, while quite rare, are remarkably well-suited to addressing outstanding issues in both galaxy evolution and fundamental physics. However, in order to study the mass distribution, methods relying on hydrostatic (X-rays) or dynamical equilibrium are ill-suited for such systems.

We have applied a mass reconstruction method based on strong and weak gravitational lensing to the cluster 1E0657–56. We use deep, high resolution optical data to identify objects belonging to the same multiple-image systems. The same data are used to obtain weak lensing catalogs allowing us to obtain a strong+weak lensing mass map of the cluster core. Our main conclusions are the following:

1. Using the combined strong and weak lensing mass reconstruction we derive a high-resolution, absolutely calibrated mass map; we get projected, enclosed mass $M_{\text{main}}(< 250 \text{ kpc}) = (2.8 \pm 0.2) \times 10^{14} M_{\odot}$ around the main and $M_{\text{sub}}(< 250 \text{ kpc}) = (2.3 \pm 0.2) \times 10^{14} M_{\odot}$ around the subcluster.
2. We detect the main cluster peak and a distinct mass concentration at the subcluster position, both clearly offset from the location of the X-ray gas in the system (at $10\text{-}\sigma$ and $6\text{-}\sigma$ significance for the main and the subcluster respectively - see Fig. 4 and Tab. 2).
3. The majority of the mass is spatially coincident with the galaxies, which implies that the cluster mass must be dominated by a relatively collisionless form of dark matter. The high resolution data allow us to significantly detect the shapes of both the main mass component and the subcluster with no prior assumptions on their positions or profiles.

We show that the cluster 1E0657–56 is a very efficient strong lens; the area enclosed within the critical curve for highest redshift sources is comparable to that of A1689 Broadhurst et al. (2005). Consequently, we plan to conduct a pencil beam survey for high-redshift ($z \sim 7$) objects. At present this is not possible, because we lack both reliable redshift information for the 1E0657–56 multiple image systems, and multi-color high-resolution imaging data in the main cluster region. The latter is

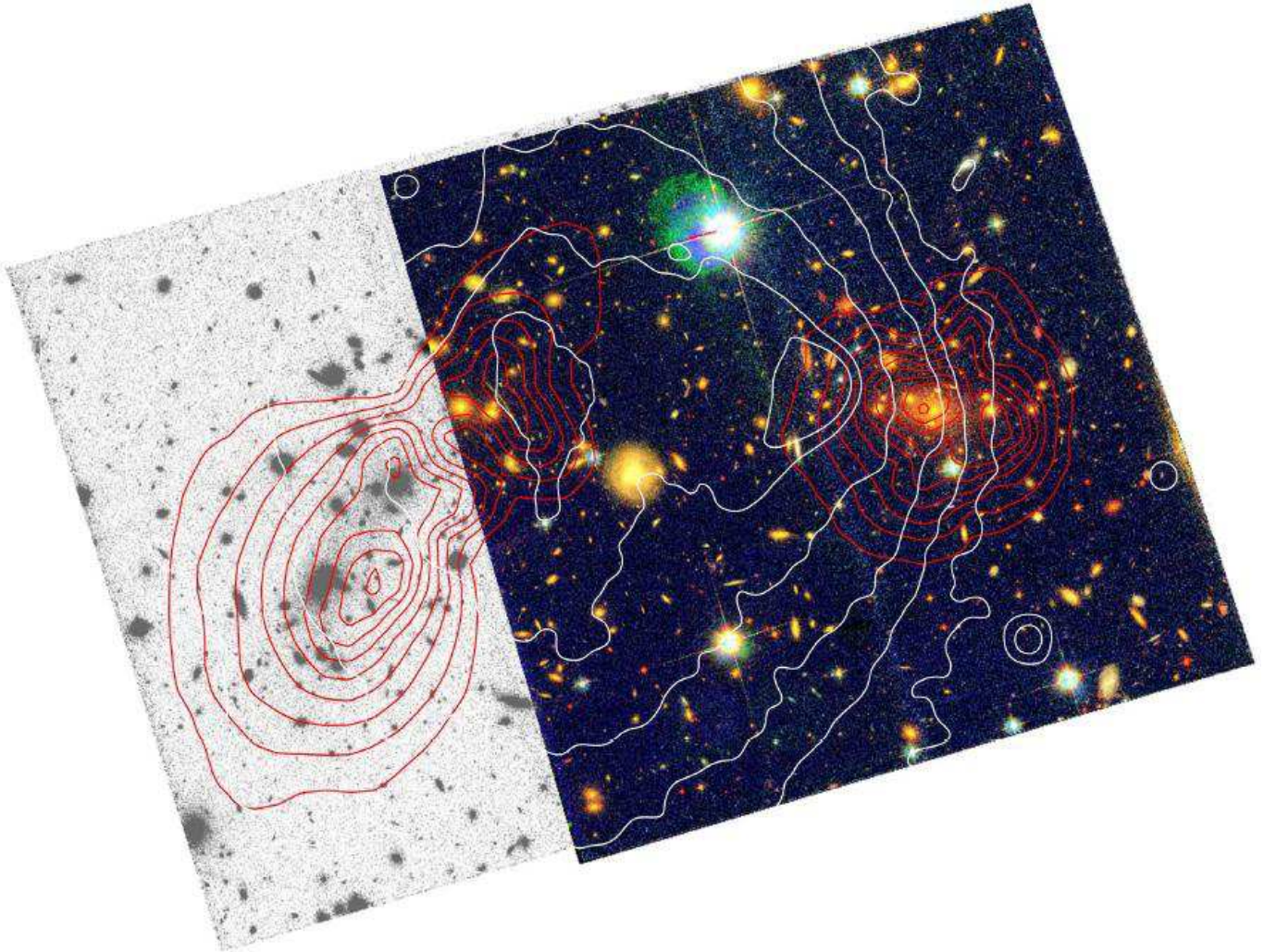


FIG. 4.— The F435W-F606W-F814 color composite of the cluster 1E0657–56. Overlaid in *red contours* is the surface mass density κ from the combined weak and strong lensing mass reconstruction (for the purpose of this plot we recalculate the final κ -map from top-left panel of Fig. 6 on a finer grid). The contour levels are linearly spaced with $\Delta\kappa = 0.1$, starting at $\kappa = 0.5$, for a fiducial source at a redshift of $z_s \rightarrow \infty$. The X-ray brightness contours from the 500 ks Chandra ACIS-I observations (Markevitch et al. 2006) are overlaid in *white*. North is up and East is left, the field is $4.9' \times 3.2'$, which corresponds to 1300×830 kpc² at the redshift of the cluster. The color composite was created following the algorithm from Lupton et al. (2004).

TABLE 3

COMPARISON BETWEEN THE GAS MASS AND THE TOTAL MASS FOR FOUR ELLIPTICAL REGIONS CENTERED ON THE MAXIMA OF THE GAS DENSITY MAP AND THE SOUTHERN cD / BCG OF THE MAIN / SUBCLUSTER. R_a AND R_b INDICATE SEMI-MAJOR AND SEMI-MINOR AXES (R_a IS ORIENTED W.R.T. RA) OF THE REGION CONSIDERED. LAST ROW GIVES THE CORRESPONDING NUMBERS FOR THE ENTIRE ACS FIELD (RECTANGLE).

	$R_a \times R_b$ [kpc] ([arcmin])	$M_{\text{gas}} [10^{13} M_{\odot}]$	$M_{\text{total}} [10^{13} M_{\odot}]$	$M_{\text{gas}} / M_{\text{total}}$
Main (gas peak)		2.0 ± 0.2	10.8 ± 0.6	0.19 ± 0.03
Main (S cD)	$125 (0.47) \times 250 (0.59)$	1.4 ± 0.1	16.3 ± 0.9	0.09 ± 0.01
Sub (gas peak)		0.42 ± 0.04	2.1 ± 0.2	0.20 ± 0.06
Sub (BCG)	$80 (0.31) \times 80 (0.31)$	0.18 ± 0.02	4.3 ± 0.2	0.04 ± 0.01
ACS field	$1300 (4.9) \times 830 (3.2)$	13 ± 1	91 ± 10	0.14 ± 0.03

needed to identify counter images for the strong lens systems, and so improve the reliability of the mass map to the south-east of the main cluster. Once these data are obtained (HST Cycle 15), we will improve our method-

ology to include an adaptive grid approach, which will greatly improve the constraints on the location of critical curves for these high-redshift sources.

The prospects for such a search are however very

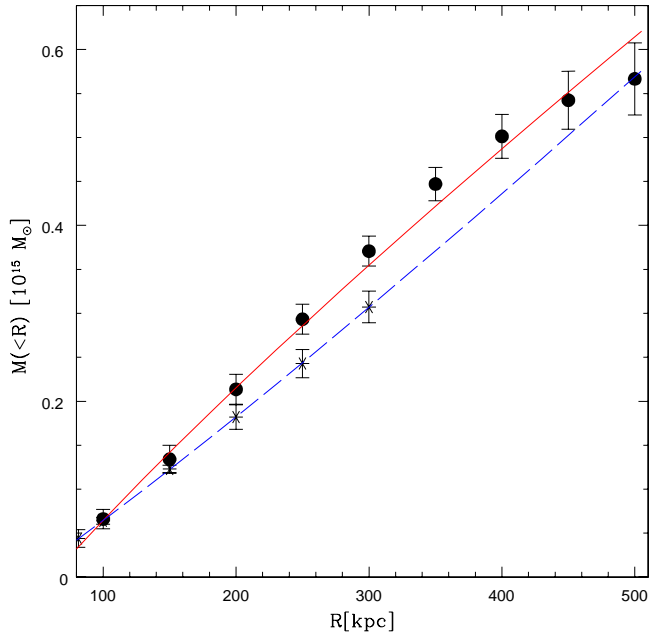


FIG. 5.— The integrated mass profile of 1E0657–56. The profile was determined by measuring the enclosed mass in cylinders, centered on the southern cD of the main cluster (dots), and the BCG of the subcluster (crosses). We fit power law profiles to the data $M(<R) \propto R^{\alpha}$, the results are shown for the main (solid line) and for the subcluster (dashed line).

promising, as we already have two strong candidate high redshift objects. One is the red arc B, which is constrained to lie at $3.24 < z < 6$ based upon the redshift of arc A and detection in F814W. The other (see Fig. 8)

is Spitzer IRAC-selected with a likely redshift of $z \gtrsim 6$. Using this cluster as a gravitational telescope will therefore allow us to study galaxy properties near the epoch of reionization.

The high resolution mass map of this cluster, in addition to enabling the high- z galaxy search, will be valuable for several other ongoing science programs. Most significantly, we are currently running simulations to reconstruct the dynamical history of the cluster merger, and provide an independent constraint on the dark matter self-interaction cross-section. The relative masses of the main and the subcluster, and the central mass distribution, two critical parameters for the simulations, were the limiting source of uncertainty prior to this work.

We would like to thank Marco Lombardi, Roger Blandford, Peter Schneider, and Steve Allen for many useful discussions that helped to improve the paper, and Mischa Schirmer for producing the color image used for Fig. 9. We are grateful to the anonymous referee for valuable comments and suggestions that helped to improve this manuscript, and for pointing out a typo in our previous paper of the series. Further we would like to thank Volker Springel for providing us with the simulations used in the paper. Support for this work was provided by NASA through grant number HST-GO-10200.05-A from the Space Telescope Science Institute, which is operated by AURA, Inc., under NASA contract NAS 5-26555. MB acknowledges support from the NSF grant AST-0206286. This project was partially supported by the Department of Energy contract DE-AC3-76SF00515 to SLAC. DC and DZ acknowledge support from NASA through grant number LTSA04-0000-0041. MM acknowledges support from Chandra grant GO4-5152X.

REFERENCES

- Barrena, R., Biviano, A., Ramella, M., Falco, E. E., & Seitz, S. 2002, *A&A*, 386, 816
- Bartelmann, M. & Schneider, P. 2001, *Phys. Rep.*, 340, 291
- Bertin, E. & Arnouts, S. 1996, *A&AS*, 117, 393
- Bradač, M., Erben, T., Schneider, P., Hildebrandt, H., Lombardi, M., Schirmer, M., Schindler, S., & Miralles, J.-M. 2005a, *A&A*, 437, 49
- Bradač, M., Lombardi, M., & Schneider, P. 2004, *A&A*, 424, 13
- Bradač, M., Schneider, P., Lombardi, M., & Erben, T. 2005b, *A&A*, 437, 39
- Brainerd, T. G., Blandford, R. D., & Smail, I. 1996, *ApJ*, 466, 623
- Broadhurst, T., Benítez, N., Coe, D., Sharon, K., Zekser, K., White, R., Ford, H., et al. 2005, *ApJ*, 621, 53
- Clowe, D., Bradac, M., Gonzalez, A., Markevitch, M., Randall, S., Jones, C., & Zaritsky, D. 2006a, Accepted *ApJL*
- Clowe, D., Gonzalez, A., & Markevitch, M. 2004, *ApJ*, 604, 596
- Clowe, D., Schneider, P., Aragón-Salamanca, A., Bremer, M., de Lucia, G., Halliday, C., Jablonka, P., Milvang-Jensen, B., Pelló, R., Poggianti, B., Rudnick, G., Saglia, R., Simard, L., White, S., & Zaritsky, D. 2006b, *A&A*, 451, 395
- Clowe, D. et al. 2006c, in preparation
- Fontana, A., D’Odorico, S., Fosbury, R., Giallongo, E., Hook, R., Poli, F., Renzini, A., et al. 1999, *A&A*, 343, L19
- Gomez, P., Romer, A. K., Peterson, J. B., Chase, W., Runyan, M., Holzappel, W., Kuo, C. L., et al. 2004, in *AIP Conf. Proc. 703: Plasmas in the Laboratory and in the Universe: New Insights and New Challenges*, 361–366
- Hayashi, E. & White, S. D. M. 2006, *ArXiv Astrophysics e-prints*
- Heymans, C., Brown, M. L., Barden, M., Caldwell, J. A. R., Jahnke, K., Peng, C. Y., Rix, H.-W., Taylor, A., Beckwith, S. V. W., Bell, E. F., Borch, A., Häußler, B., Joojee, S., McIntosh, D. H., Meisenheimer, K., Sánchez, S. F., Somerville, R., Wisotzki, L., & Wolf, C. 2005, *MNRAS*, 361, 160
- Heymans, C., Van Waerbeke, L., Bacon, D., Berge, J., Bernstein, G., Bertin, E., Bridle, S., Brown, M. L., Clowe, D., Dahle, H., Erben, T., Gray, M., Hettterscheidt, M., Hoekstra, H., Hudelot, P., Jarvis, M., Kuijken, K., Margoniner, V., Massey, R., Mellier, Y., Nakajima, R., Refregier, A., Rhodes, J., Schrabback, T., & Wittman, D. 2006, *MNRAS*, 368, 1323
- Jee, M. J., White, R. L., Ford, H. C., Illingworth, G. D., Blakeslee, J. P., Holden, B., & Mei, S. 2006, *ApJ*, 642, 720
- Kaiser, N., Squires, G., & Broadhurst, T. 1995, *ApJ*, 449, 460
- Keeton, C. & Kochanek, C. 1998, *ApJ*, 495, 157
- Kneib, J.-P., Ellis, R. S., Smail, I., Couch, W. J., & Sharples, R. M. 1996, *ApJ*, 471, 643
- Kochanek, C. S. 2004, *astro-ph/0407232*
- Koekemoer, A. M., Fruchter, A. S., Hook, R. N., & Hack, W. 2002, in *The 2002 HST Calibration Workshop*, Baltimore, MD, 2002., p.339, 339
- Lupton, R., Blanton, M. R., Fekete, G., Hogg, D. W., O’Mullane, W., Szalay, A., & Wherry, N. 2004, *PASP*, 116, 133
- Markevitch, M., Gonzalez, A. H., Clowe, D., Vikhlinin, A., Forman, W., Jones, C., Murray, S., & Tucker, W. 2004, *ApJ*, 606, 819
- Markevitch, M., Gonzalez, A. H., David, L., Vikhlinin, A., Murray, S., Forman, W., Jones, C., & Tucker, W. 2002, *ApJ*, 567, L27
- Markevitch, M. et al. 2006, in preparation
- Mehlert, D., Seitz, S., Saglia, R. P., Appenzeller, I., Bender, R., Fricke, K. J., Hoffmann, T. L., et al. 2001, *A&A*, 379, 96
- Randall, S. et al. 2006, in preparation
- Springel, V., White, S. D. M., Tormen, G., & Kauffmann, G. 2001, *MNRAS*, 328, 726
- Tucker, W. H., Tananbaum, H., & Remillard, R. A. 1995, *ApJ*, 444, 532

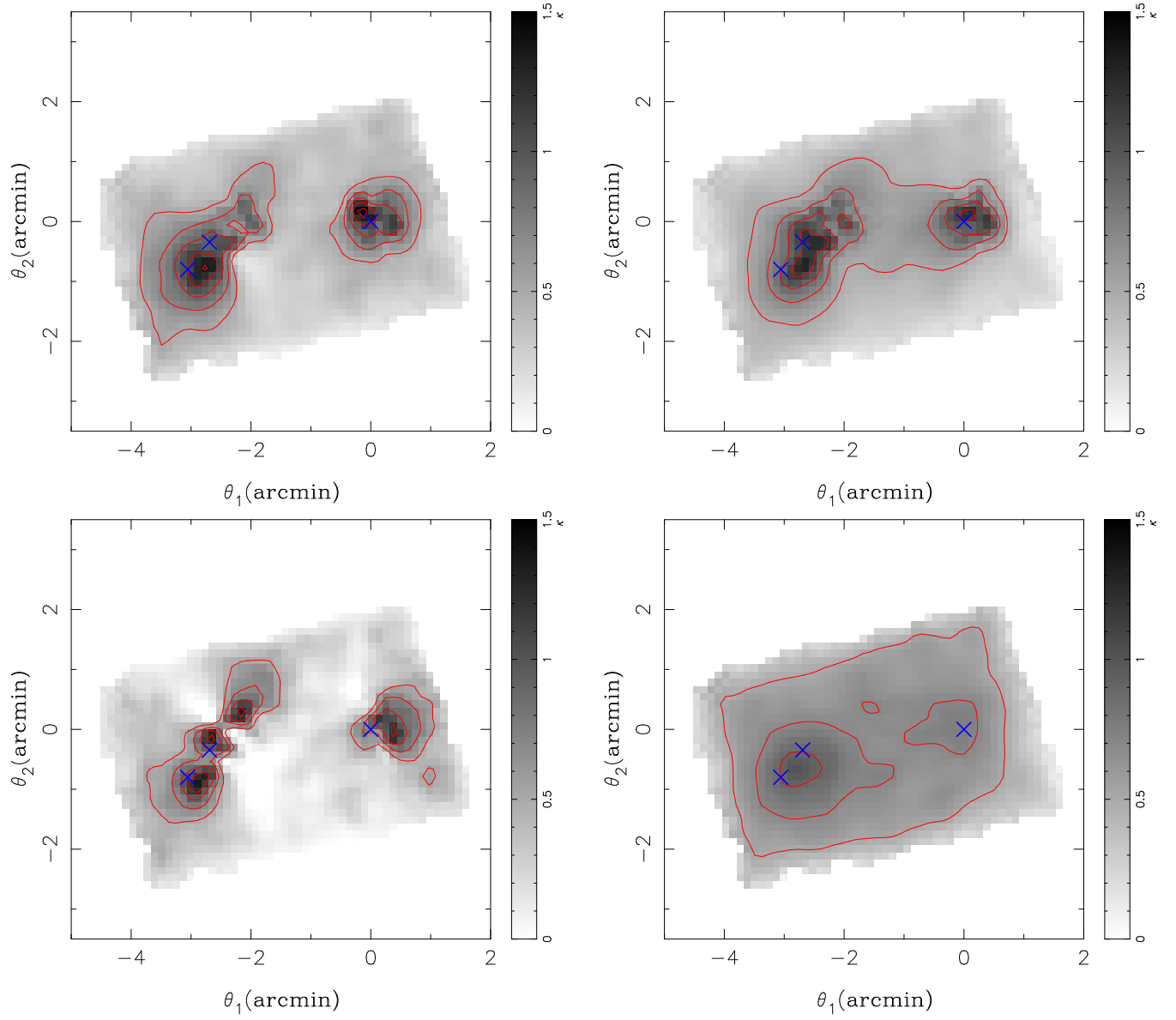


FIG. 6.— The effects of different initial conditions (a-c) and exclusion of the strong lensing data (d) on the final reconstruction. Shown is the surface mass density κ of the weak and strong lensing reconstruction using the two component NIE model (*top-left*) as initial guess, using weak lensing reconstruction from Clowe et al. (2006a) (*top-right*), and using zero initial model (*bottom-left*). The weak lensing only mass reconstruction is shown in (*bottom-right*); all for a fiducial source at a redshift of $z_s \rightarrow \infty$. The contour levels are linearly spaced with $\Delta\kappa = 0.2$, starting at $\kappa = 0.5$. The two cD's and the BCG of the subcluster are denoted with crosses.

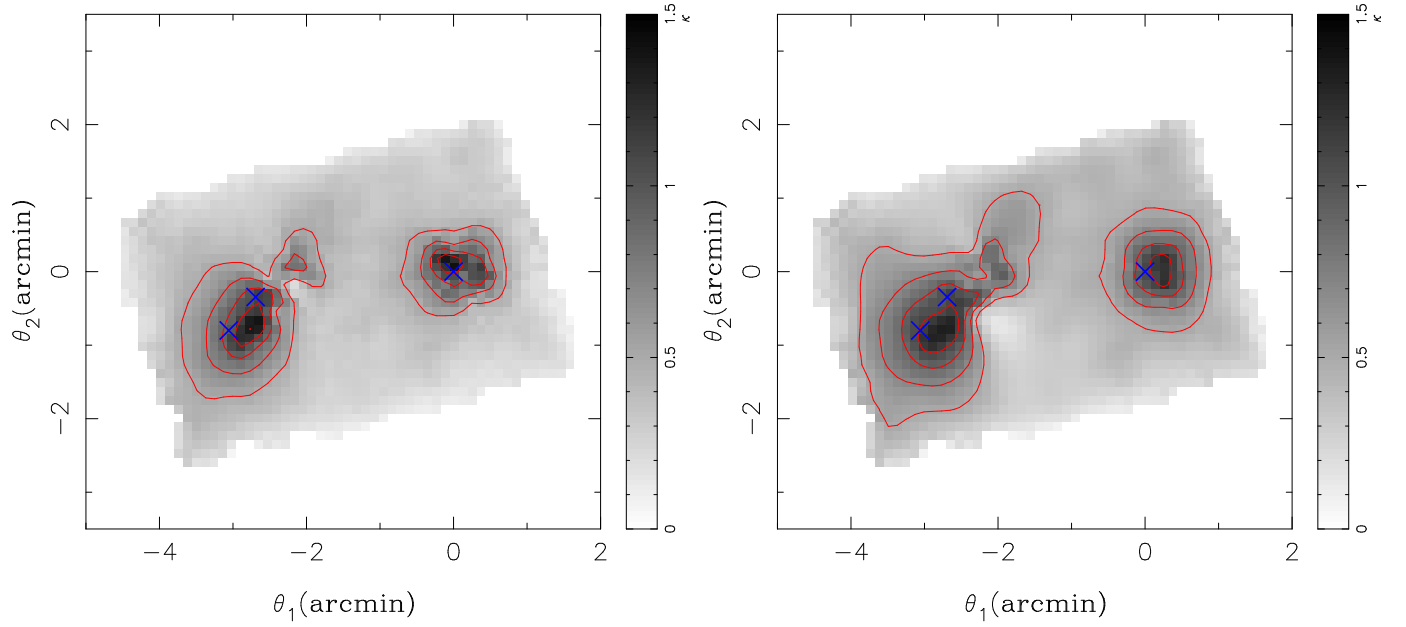


FIG. 7.— The surface mass density κ of the two reconstructions where we (*left*) removed image system D, and (*right*) image system I from the data. These are two extreme examples where the resulting χ^2 decreased at most; still the resulting maps are very similar to the original reconstruction. The contour levels are the same as in Fig. 6, the two cD's of the main and the BCG of the subcluster are denoted with crosses.

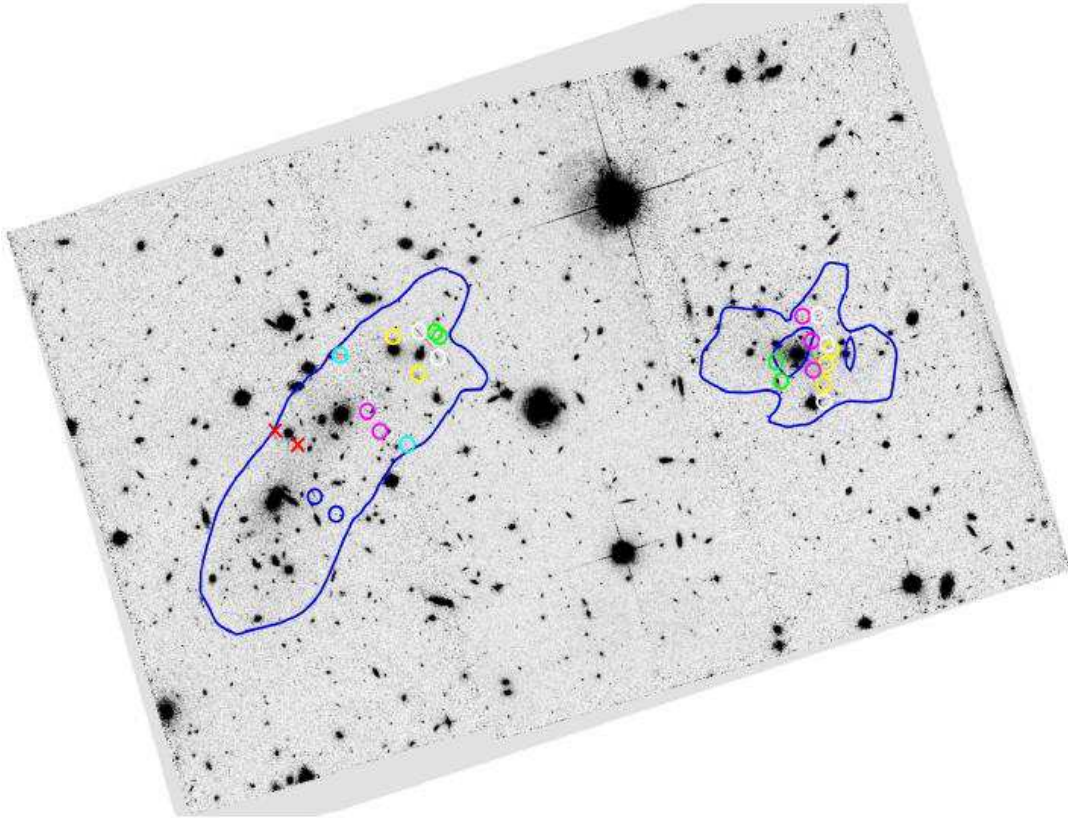


FIG. 8.— The critical curve for a fiducial source at $z \rightarrow \infty$ from the combined strong and weak lensing reconstruction. Circles denote the positions of the multiple image systems we used, while the crosses denote the candidate high redshift source identified using Spitzer data (note that this system was *not* included in the reconstruction). North is up and East is left, the field is $4.9' \times 3.2'$.

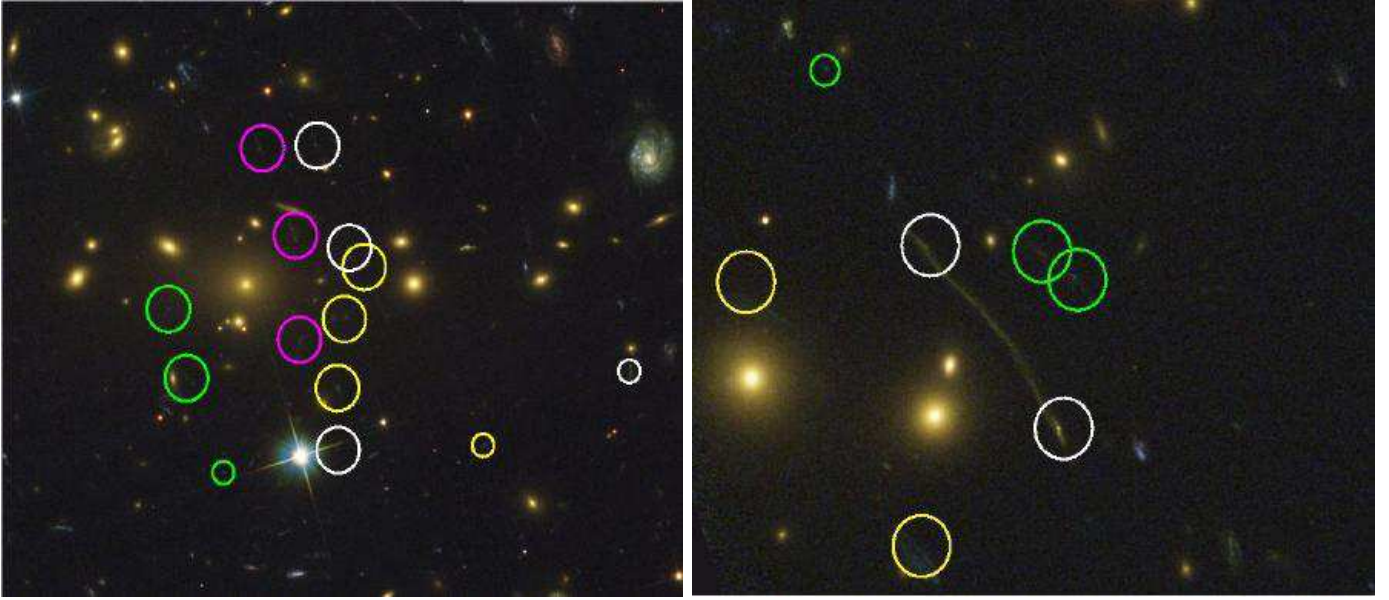


FIG. 9.— The F435W-F606W-F814W color composite of the $1.1' \times 0.9'$ inner part of the subcluster (*left*) and of the $0.6' \times 0.5'$ cutout around arc B (*right*) with large circles denoting the positions of the multiple image systems we used. The small circles show the candidate counter images as predicted by the weak and strong lensing reconstruction (not used in the final reconstruction). Image courtesy of Mischa Schirmer.